

# Self-Doping and Electrical Conductivity in Spinel Oxides: Experimental Validation of Doping Rules

Yezhou Shi,<sup>†</sup> Paul F. Ndione,<sup>‡</sup> Linda Y. Lim,<sup>†</sup> Dimosthenis Sokaras,<sup>†</sup> Tsu-Chien Weng,<sup>†</sup> Arpun R. Nagaraja,<sup>§</sup> Andreas G. Karydas,<sup>||,⊥</sup> John D. Perkins,<sup>‡</sup> Thomas O. Mason,<sup>§</sup> David S. Ginley,<sup>‡</sup> Alex Zunger,<sup>#</sup> and Michael F. Toney<sup>\*,†</sup>

<sup>†</sup>SLAC National Accelerator Laboratory, Menlo Park, California 94025, United States

<sup>‡</sup>National Renewable Energy Laboratory, Golden, Colorado 80401, United States

<sup>§</sup>Northwestern University, Evanston, Illinois 60208, United States

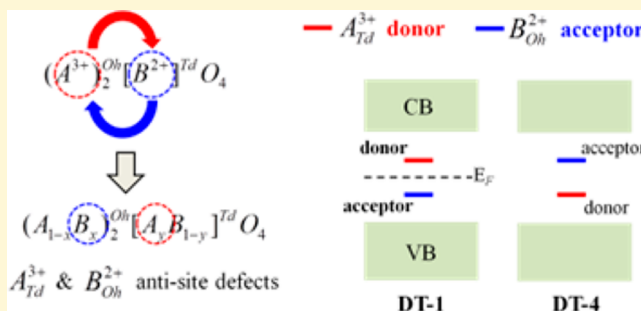
<sup>||</sup>NCSR Demokritos, Institute of Nuclear Physics, GR-15310, Athens, Greece

<sup>⊥</sup>Nuclear Science and Instrumentation Laboratory, IAEA Laboratories, Austria A-2444, Seibersdorf, Austria

<sup>#</sup>University of Colorado at Boulder, Boulder, Colorado 80309, United States

## Supporting Information

**ABSTRACT:** Self-doping of cations on the tetrahedral and octahedral sites in spinel oxides creates “anti-site” defects, which results in functional optical, electronic, magnetic, and other materials properties. Previously, we divided the III–II spinel family into four doping types (DTs) based on first-principle calculations in order to understand their electrical behavior. Here, we present experimental evidence on two prototype spinels for each major doping type (DT1 and DT4) that test the first principles calculations. For the DT-1 Ga<sub>2</sub>ZnO<sub>4</sub> spinel, we show that the anti-site defects in a stoichiometric film are equal in concentration and compensate each other, whereas, for nonstoichiometric Cr<sub>2</sub>MnO<sub>4</sub>, a representative DT-4 spinel, excess Mn on the tetrahedral sites becomes electrically inactive as the Mn species switch from (III) to (II). The agreement between experiment and theory validates the Doping Rules distilled from the theoretical framework and significantly enhances our understanding of the defect chemistry of spinel oxides.



## 1. INTRODUCTION

Despite the opportunities to utilize ternary spinel oxides as functional materials, one barrier to their widespread use for electronic applications is understanding their electrical properties by traditional defect chemistry.<sup>1,2</sup> These oxides have a general chemical formula A<sub>2</sub>BO<sub>4</sub>, with A and B cations occupying two inequivalent lattice sites: one with four tetrahedrally (*Td*) coordinated nearest neighbor oxygen atoms and one with six octahedrally (*Oh*) coordinated oxygens.<sup>3</sup> Due to the possibility of accommodating earth-abundant transition metals in different oxidation states at the *Td* and *Oh* sites, spinels offer an excellent opportunity for designing functional materials, such as transparent conducting oxides (TCOs),<sup>4–6</sup> electrodes in lithium-ion<sup>7</sup> and sodium-ion batteries,<sup>8</sup> magnetic materials for storage<sup>9</sup> and spintronics,<sup>10</sup> and hydrogen generation for microbial systems,<sup>11</sup> redox materials for solar-thermal water splitting,<sup>12</sup> as well as high surface-reactivity catalysts for water-gas shift reactions.<sup>13</sup> In a “normal” A<sub>2</sub>BO<sub>4</sub> spinel oxide, all A cations occupy the *Oh* sites whereas the B cations occupy *Td* sites, while, in an “inverse” spinel, the *Oh* sites are shared equally by A and B cations with

the *Td* sites occupied only by A cations. The A cations often have an oxidation state of (III) and the B cations an oxidation state of (II). Spinel with A(II) and B(IV) are also of interest but have not been classified yet by theory.

Point defects influence the electronic properties through the generation of charge carriers, and recent results show that electronic and optical properties in spinels are related to *anti-site defects* (e.g., cations that usually occupy *Td* sites reside on *Oh* sites or vice versa) created by cross-substitution of the A and B cations. Recent theoretical and experiment advances show that, unlike many binary oxides, where oxygen vacancies or cation interstitial defects are prevalent, predicted by conventional solid state defect chemistry,<sup>14</sup> doping in ternary spinel is a matter of *anti-site defects* created by self-doping or cross-substitution. The defect formation energy of oxygen vacancies is considerably higher than the anti-site defects in III–II spinels<sup>16</sup> and the oxygen vacancies concentrations are

Received: December 8, 2013

Revised: February 1, 2014

Published: February 12, 2014

unlikely to appear in appreciable concentrations ( $>10^{16} \text{ cm}^{-3}$ ) without reductive treatment. For example, in inverse  $(\text{FeNi})^{\text{Oh}}\text{Fe}^{\text{Td}}\text{O}_4$  thin films, anti-site  $\text{Ni}_{\text{Td}}$  and  $\text{Fe}_{\text{Oh}}$  defects break the magnetic compensation of  $\text{Fe}_{\text{Oh}}$  and  $\text{Fe}_{\text{Td}}$  and enhance the magnetization.<sup>10</sup> Furthermore, external doping of Cr(III) for Ni(II) on the *Oh* sites in  $\text{Li}(\text{I})\text{Ni}(\text{II})_{0.5}\text{Mn}(\text{IV})_{1.5}\text{O}_4$  induces Mn(III) defect states which improve  $\text{Li}^+$  transport and the overall performance of this spinel as the cathode in Li-ion batteries.<sup>15</sup>

The central theoretical insight pertaining to spinel dopability<sup>16</sup> is indicated in Table 1, which shows possible

**Table 1. Possibilities for the Formation of Donor or Acceptor States Depending on the Position and Oxidation States of the Cations**

dopant	host site	
	tetrahedral site ( <i>Td</i> )	octahedral site ( <i>Oh</i> )
B cation	no donor no acceptor	<b>acceptor if B(II)</b> nothing if B(III)
A cation	<b>donor if A(III)</b> nothing if A(II)	no donor no acceptor

donor and acceptor states in III–II spinels. As long as all  $\text{B}^{2+}$  ions substitute the *Td* site and all  $\text{A}^{3+}$  ions substitute the *Oh* site, the system stays insulating and no carriers are introduced. Doping occurs from *off diagonal* entries in Table 1 (indicated by bold). Specifically, if  $\text{A}^{3+}$  cations substitute on the *Td* site and stay in the (III) oxidation state, they will form electron-producing donors, making the system *n*-type. Analogously, if the  $\text{B}^{2+}$  cations substitute the *Oh* site and stay in their (II) oxidation state, they will form hole-producing acceptors, making the system *p*-type. If such donors and acceptors were created simultaneously in equivalent quantities, they would compensate each other electrically, and no doping would occur. This immediately suggests that dopability in normal III–II spinels depends on designing imperfect compensation by donors and acceptors or, more generally, by controlling site occupancy. Here we examine, via site-occupancy sensitive measurements, this theoretical insight pertaining to control of doping.

As Table 1 shows, the first-principles derived grouping into four different doping types (DTs) for the III–II spinels is based on the relative positions of the anti-site defect energy levels ( $A_{\text{Td}}$  as the potential donor with energy level  $E_{\text{D}}$  and  $B_{\text{Oh}}$  as the acceptor with energy level  $E_{\text{A}}$ ).<sup>16</sup> In DT-1 spinels, the donor states  $A_{\text{Td}}$  ( $E_{\text{D}}$ ) lie above the  $B_{\text{Oh}}$  acceptor states ( $E_{\text{A}}$ ), both within the band gap. Electrical compensation is possible and the conductivity depends on the materials details, e.g., stoichiometry. For DT-2,  $E_{\text{D}}$  ( $A_{\text{Td}}$  level) is in the valence band and is below  $E_{\text{A}}$  ( $B_{\text{Oh}}$  level) in the band gap, and there is *p*-type conductivity:  $B_{\text{Oh}}$  produces holes, but  $A_{\text{Td}}$  is neutral. In DT-3, this is reversed ( $E_{\text{A}}$  is in the conduction band and lies above  $E_{\text{D}}$  in the band gap). The spinel is *n*-type. Last, for DT-4 spinels, both  $E_{\text{A}}$  and  $E_{\text{D}}$  are in the gap with  $E_{\text{D}}$  below  $E_{\text{A}}$  ( $A_{\text{Td}}$  level lower than  $B_{\text{Oh}}$  level). Neither donor nor acceptor can be effectively ionized and DT-4 spinels are always insulating, although extrinsic doping can lead to *p*- or *n*-type conductivity. A Kröger-Vink notation for the DTs can be found in the Supporting Information (SI).

We have shown that, for a representative DT-2  $\text{Co}_2\text{ZnO}_4$ , the *p*-type behavior resulted from the positively charged  $\text{Zn}_{\text{Oh}}$  states whereas the anti-site defect  $\text{Co}_{\text{Td}}$  formed easily yet remained

electrically neutral,<sup>17,18</sup> consistent with the DT model. While we have experimentally validated one of the four DTs, a complete experimental assessment of the theory is lacking and is the goal of this research. Employing resonant elastic X-ray diffraction (REXD), X-ray absorption spectroscopy (XAS), and X-ray emission spectroscopy (XES), we examine the *site-specific* cation occupancies and oxidation states in biaxially textured  $\text{Ga}_2\text{ZnO}_4$  and  $\text{Cr}_2\text{MnO}_4$  films, prototype materials for DT-1 and DT-4 spinels, respectively. The agreement between experiment and theory enhances our understanding of the electrical properties in spinel oxides, which cannot be simply accounted for by invoking the concept of oxygen vacancies or cation interstitials. The doping rules can serve as guidelines for designing and making spinel oxides with targeted electrical properties ignored or unpredicted by conventional defect chemistry.

## 2. THEORETICAL CONCEPTS

Previously, we studied III–II spinels based on first-principles calculations and distilled rules that divide these oxides into the four different doping types (DTs) or classes, based on the relative position of the anti-site defect energy levels.<sup>16</sup> The Supporting Information contains more details on this classification, including a schematic of the DTs.

**The DT-1 doping situation** (e.g.,  $\text{Ga}_2\text{ZnO}_4$ ,  $\text{In}_2\text{MnO}_4$ , and  $\text{Ga}_2\text{CuO}_4$ ) occurs when the acceptor level resulting from  $\text{B}^{2+}$  substituting the *Oh* site lies energetically *below* the donor level resulting from  $\text{A}^{3+}$  substituting the tetrahedral site and both levels are in the gap. This means that the A cation retains its natural 3+ charge even though its now substituting a *Td* site, and the B cation retains its natural 2+ charge even though it now resides on the *Oh* site. This is a classic donor–acceptor compensation situation; the precise degree of compensation depends on the relative concentration of the donors and acceptors. The critical feature of the DT-1 level arrangement is that both native donors and native acceptors are active so there is natural opposition to intrinsic or extrinsic *n*-type and *p*-type doping. Here, we show that the experiments agree well with first principles predictions for prototypical  $\text{Ga}_2\text{ZnO}_4$ , with electrically active, but compensating anti-site defects ( $\text{Ga}_{\text{Td}}$  and  $\text{Zn}_{\text{Oh}}$ ).

**The DT-2 doping situation** (e.g.,  $\text{Co}_2\text{ZnO}_4$ ,  $\text{Rh}_2\text{CoO}_4$ , and  $\text{Ir}_2\text{MgO}_4$ ) occurs when the acceptor level resulting from  $\text{B}^{2+}$  substituting the octahedral site lies energetically in the gap and *above* the donor level resulting from  $\text{A}^{3+}$  substituting the tetrahedral site, and the latter is inside the valence band. This means that the A cation *loses* its natural (III) charge when it substitutes a *Td* site, becoming (II); that is, it is electrically neutral. At the same time, the B cation retains its natural (II) charge even though it now resides on the *Oh* site, making it an effective hole-producing acceptor. The critical feature of the DT-2 level arrangement is that native donors are inactive so there is no natural opposition to either intrinsic or extrinsic *p*-type doping. This DT-2 behavior was previously verified in  $\text{Co}_2\text{ZnO}_4$  with the *p*-type conductivity.<sup>17,19</sup> We have shown that, for a representative DT-2  $\text{Co}_2\text{ZnO}_4$ , the *p*-type behavior resulted from the positively charged  $\text{Zn}_{\text{Oh}}$  states,<sup>18</sup> while, in equilibrium materials, the anti-site defect  $\text{Co}_{\text{Td}}$  formed easily but remained electrically neutral,<sup>17</sup> consistent with the DT-2 behavior.

**The DT-3 doping situation** (no examples) occurs when the acceptor level resulting from  $\text{B}^{2+}$  substituting the *Oh* site lies energetically inside the conduction band and *above* the donor

Table 2. Target Composition, Film Composition, Site Occupancy, and Average Mn Oxidation State for CMO Films<sup>a</sup>

target composition	film composition (XRF)	site occupancies (REXD)	calc Mn ox. states (REXD)	avg Mn ox. states (XANES)	avg Mn ox. states (XES)
Cr <sub>2</sub> MnO <sub>4</sub>	Cr <sub>1.83</sub> Mn <sub>1.17</sub> O <sub>4</sub>	(Cr <sub>0.85</sub> Mn <sub>0.15</sub> ) <sub>2</sub> <sup>Oh</sup> Mn <sup>Td</sup> O <sub>4</sub> Cr <sub>1.7</sub> Mn <sub>1.3</sub> O <sub>4</sub>	2.23 ± 0.02	2.13 ± 0.12	2.25 ± 0.04
Cr <sub>1.5</sub> Mn <sub>1.5</sub> O <sub>4</sub>	Cr <sub>1.33</sub> Mn <sub>1.67</sub> O <sub>4</sub>	(Cr <sub>0.70</sub> Mn <sub>0.30</sub> ) <sub>2</sub> <sup>Oh</sup> Mn <sup>Td</sup> O <sub>4</sub> Cr <sub>1.4</sub> Mn <sub>1.6</sub> O <sub>4</sub>	2.38 ± 0.03	2.26 ± 0.11	2.33 ± 0.04

<sup>a</sup>The error bars on the site occupancies are stated in the text but are approximately 0.02–0.03. The composition from the REXD data is stated in the row below the site occupancy; this is the composition used to describe the films in the text.

gap level that results from A<sup>3+</sup> substituting the tetrahedral site. This means that the A cation retains its natural 3+ charge even though it is now substituting a Td site (thus, A is an effective donor), whereas the B cation loses its natural (II) charge on the Oh site, becoming (III) and therefore electrically neutral. While the net carrier concentration depends, as usual, on the relative concentrations of donors and acceptors, the DT-3 situation would lead to *n*-type behavior. The critical feature of the DT-3 level arrangement is that native acceptors are inactive so there is no natural opposition to either intrinsic or extrinsic *n*-type doping. No DT-3 materials have been identified for known III–II spinels.

**The DT-4 doping situation** (e.g., Cr<sub>2</sub>MnO<sub>4</sub> and Cr<sub>2</sub>CoO<sub>4</sub>) occurs when the acceptor level resulting from B<sup>2+</sup> substituting the octahedral site lies energetically *inside the band gap* and still (as in DT-3) *above* the donor level that results from A<sup>3+</sup> substituting the tetrahedral site. This means that the A cation loses its natural (III) charge as it substitutes a Td site (thus, A is electrically neutral), and the B cation loses its natural (II) charge on the Oh site, becoming (III) (thus B is also electrically neutral). Whereas the net carrier concentration depends, as usual, on the relative concentrations of donors and acceptors, DT-4 should generically lead to intrinsic charge neutrality, setting the stage for extrinsic doping without opposition by native donors or acceptors. We demonstrate this DT-4 behavior in nonstoichiometric Cr<sub>2</sub>MnO<sub>4</sub> films, where Mn(II) becomes Mn(III) on the O<sub>h</sub> sites rendering the nondoped system electrically inactive.

### 3. EXPERIMENTAL SECTION

**3.1. Sample Fabrication and Characterization.** Bulk spinel oxides possess relatively low concentration of anti-site defects (10<sup>22</sup> cm<sup>-3</sup> or below 1% of the lattice sites), making it experimentally challenging to measure. Therefore, we chose thin film growth to achieve nonequilibrium defect concentrations. There are two possible ways to enhance the generation of anti-site defects in spinels that assume a normal configuration in equilibrium: (1) stoichiometric thin film grown under nonequilibrium conditions so cations occupy anti-site defects, and (2) nonstoichiometric films (different from A<sub>2</sub>BO<sub>4</sub>) with one of the cations exceeding stoichiometric concentration and residing on its anti-sites. Pulsed laser deposition (PLD) was used to fabricate biaxially textured thin films for both Ga–Zn–O (GZO) and Cr–Mn–O (CMO) on single crystal SrTiO<sub>3</sub> (001)-oriented substrates. For GZO, we prepared one stoichiometric film, because a slight deviation from stoichiometry leads to the formation of secondary phases of Ga<sub>2</sub>O<sub>3</sub> or ZnO. No post-annealing in a reductive environment (e.g., in hydrogen) was performed to induce oxygen vacancies. For CMO, two films were deposited from targets of different compositions.

The samples were deposited on SrTiO<sub>3</sub> by PLD using a KRF excimer laser (Spectra-Physics) operated at 248 nm with a pulse duration of 25 ns. The deposition parameters include a fluence of approximately 2 J·cm<sup>-2</sup>, a pulse rate of 10 Hz, and a target–substrate distance of 50 mm. CMO targets were fabricated via solid-state synthesis techniques (detailed procedures available in the Supporting

Information), and the GZO target was purchased from Praxair. Prior to film deposition, the chamber base pressure was 10<sup>-7</sup> Torr and the oxygen partial pressure during deposition was 2 mTorr. The substrate surface temperature was 600 °C for GZO and 700 °C for CMO. Film thicknesses were measured using spectroscopic ellipsometry (J. A. Woollam M-2000S) as 200 nm for CMO films and 120 nm for the GZO film. A monochromatic Cu Kα radiation (wavelength 1.54 Å) X-ray diffractometer (PANalytical X'Pert materials research diffractometer) was used to examine the crystallinity and texture of the PLD-deposited films (see Figure S1 in Supporting Information). Specular scans (2θ/ω) showed only the (00L) peaks and confirm the film was textured. The electrical conductivity was determined via sheet resistance measurements with a four-point probe using a KE6221 current source and a KE2000 multimeter. Both GZO and CMO films have conductivities below 10<sup>-4</sup> S·cm<sup>-1</sup>, the measurement limit of our four-probe setup.

**3.2. Resonant Diffraction and Analysis.** The REXD was performed on a six-circle diffractometer at beamline 7-2 of the Stanford Synchrotron Radiation Lightsource (SSRL) in the SLAC National Accelerator Laboratory. The incident X-ray energy was varied with a double crystal Si(111) monochromator. A Vortex point detector was employed to measure diffracted X-ray intensity. Azimuthal φ scans for (222) and (422) reflections were performed at various energies near the absorption K edges of Cr, Mn, Zn, and Ga. X-ray absorption spectra (XAS) for the thin films were measured over the same energy range as the resonant diffraction in order to experimentally extract the anomalous scattering factors *f*<sub>1</sub> and *f*<sub>2</sub>.

**3.3. X-ray Absorption Near-Edge Spectroscopy.** Mn K edge and Cr K edge XANES measurements were performed at SSRL beamline 4-1 and beamline 4-3. The XANES spectra were recorded in the fluorescence mode for the textured films and in the transmission mode for the powder references using Lytle and ionization chamber detectors, respectively. See the Supporting Information for a complete list of the reference materials. For each sample, three to eight scans were averaged to improve the signal-to-noise ratio. The averaged spectra were background-subtracted and normalized using the software ATHENA.<sup>20</sup> Linear combination fitting to XAS results was performed with ATHENA's linear combination fitting module.

**3.4. X-ray Emission Spectroscopy.** The Mn Kβ X-ray emission spectra were acquired at SSRL beamline 6-2 using a liquid nitrogen cooled Si(311) monochromator and a Rowland circle spectrometer comprising seven spherically bent Si(440) crystal analyzers (*R* = 1 m).<sup>21</sup> For detecting the Mn Kβ lines, the spectrometer Bragg angle was scanned around 84°. The spectrometer's energy resolution (combined with the Si(311) monochromator contribution) for the energy range of interest was found to be about 0.55 eV through elastic scattering scans. The excitation energy of the incident radiation was set at 7000 eV.

### 4. RESULTS AND DISCUSSION

CMO film compositions were determined using X-ray fluorescence (XRF), and the results are presented in Table 2 with site occupancies and oxidation states. X-ray diffraction (XRD) showed that the film is biaxially textured with azimuthal rocking curve widths for the (113) peak of 3 to 4° (Figure S1 in the Supporting Information). Complete azimuthal scans for the film and substrate showed 4-fold rotational symmetry and good

orientational alignment between the two (Figure S1 in the Supporting Information). Room temperature four-point probe measurements on the CMO and GZO films showed that the electrical conductivities are less than  $10^{-4}$  S·cm<sup>-1</sup>.

Few techniques are available to determine site occupancies in thin film oxides containing transition metals with similar atomic numbers. Here, we employ resonant elastic X-ray diffraction (REXD) to quantify cation occupancies on the spinel *Td* and *Oh* sites. REXD, also known as anomalous X-ray diffraction, combines the elemental sensitivity of a spectroscopic technique with the site selectivity of diffraction. It takes advantage of the energy dependence of the anomalous scattering factors ( $f_1$  and  $f_2$ ), which is significant near an atom's absorption edges,<sup>22</sup> in the total scattering factor:  $f(Q,E) = f_0(Q) + f_1(E) + if_2(E)$ . Consequently, the diffracted X-ray intensity changes as the incident X-ray energy is varied near an absorption edge. Due to the spinel symmetry, the (422) intensities only depend on cations on *Td* sites, whereas the (222) reflections only depend on cations on *Oh* sites and the anions.<sup>23</sup>

**4.1. Doping Type 1.** First, we examined the DT-1 model spinel, Ga<sub>2</sub>ZnO<sub>4</sub>. We assume that Ga is (III) whereas Zn is (II), as observed for Ga and Zn oxides. To quantify the occupancies of the anti-site defects, Figure 1 shows REXD data for biaxially

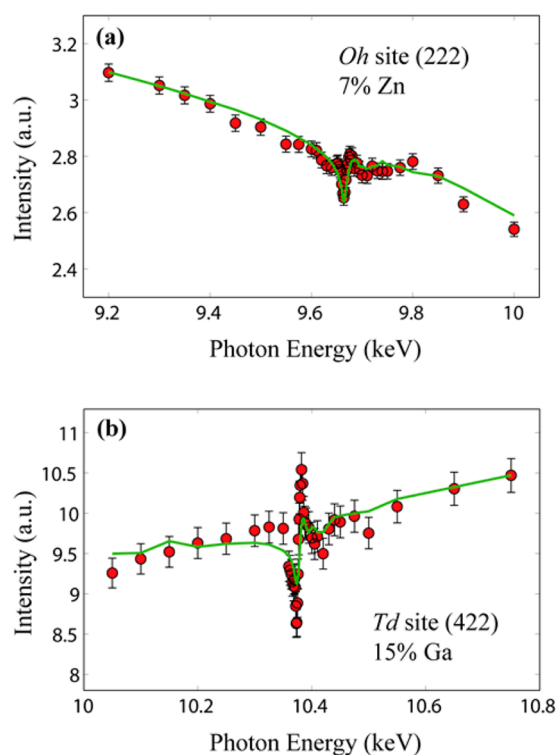


**Figure 1.** Resonant diffraction near the Zn and Ga edges (222 reflection for Zn and 422 reflection for Ga) for a stoichiometric Ga<sub>2</sub>ZnO<sub>4</sub> film. The red circles are experimental data, and the green line is the best fit. The plots are labeled with fitted site occupancies.

textured GZO taken near Zn and Ga K edges. The data were independently fit using the fraction of *Td*/*Oh* sites occupied by one cation (cation site occupancy) as a variable: Ga on the *Td* sites and Zn on the *Oh* sites for the (422) and (222) reflections, respectively. The data processing and fitting details can be found in our previous work<sup>18</sup> and in the Supporting Information. The best fit to the experimental data in Figure 1 reveals that  $7 \pm 2.5\%$  of the *Oh* sites are occupied by Zn

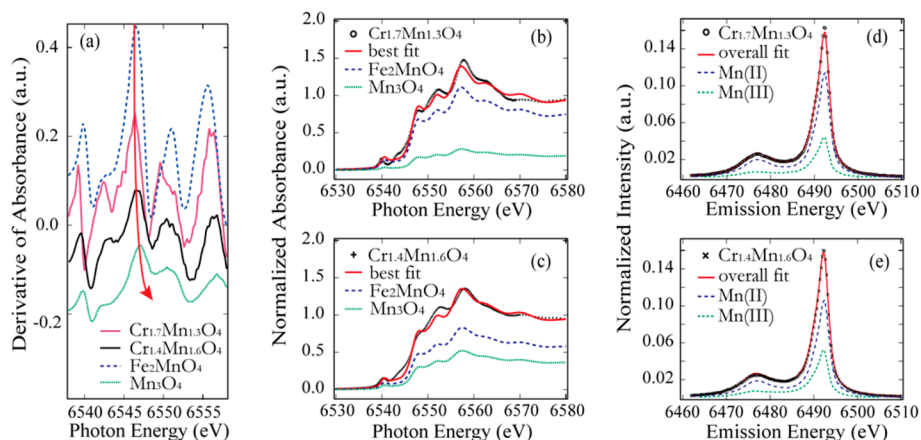
whereas  $15 \pm 5\%$  of the *Td* sites are occupied by Ga. Due to the 2:1 ratio of *Oh* to *Td* sites in spinels, the two anti-site defect concentrations are equal within experimental error. The equal concentration is predicted by the DT theory, as the two defects have similar formation enthalpies (see Figure 1 in the ref 16.). The complete charge compensation of the anti-site defects (Zn<sub>*Oh*</sub> as *p*-type and Ga<sub>*Td*</sub> as *n*-type) leads to the insulating behavior of the GZO film.

We note that DT-1 spinels are not inherently insulating, and conducting spinels in this subgroup have been reported. For example, Mn<sub>2</sub>InO<sub>4</sub> has a moderate conductivity of 0.38 S cm<sup>-1</sup>.<sup>24</sup> Neutron powder diffraction shows the difference in cation site occupancies by the anti-site defects, caused by differences in defect formation enthalpies. Within the theoretical framework of DT, we interpret these results as due to the concentration mismatch leading to incomplete charge compensation of anti-site defects, resulting in the experimentally observed conductivity.

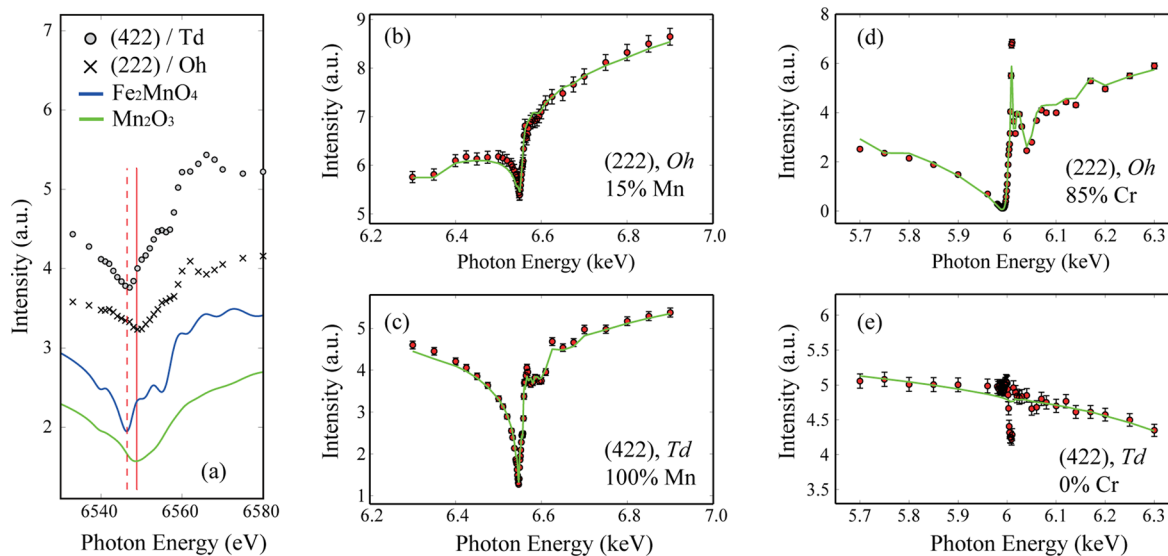
**4.2. Doping Type 4.** CMO films present a more complicated case than GZO because Cr and Mn cations possess multiple oxidation states. Table 2 summarizes the film compositions (XRF), site occupancies (REXD), and average oxidation states (XANES and XES) that we have obtained as explained below. The average oxidation states of Cr and Mn cations were determined with X-ray absorption near-edge structure (XANES) spectroscopy. The Cr species in both films are in the (III) state (see Figure S2 and Table S1 in the Supporting Information), and the similarity of the XANES between the CMO films and the Cr<sub>2</sub>FeO<sub>4</sub> reference indicates that the Cr in the CMO occupy predominantly the *Oh* sites. Thus, the XANES result is consistent with the DT theory where all Cr on the *Oh* sites are predicted to be (III).

Figure 2a presents the first derivative of the normalized XANES of the CMO films at the Mn edge. The Cr<sub>1.4</sub>Mn<sub>1.6</sub>O<sub>4</sub> film (from a nonstoichiometric Cr<sub>1.5</sub>Mn<sub>1.5</sub>O<sub>4</sub> target) has a first-derivative peak that is higher in energy than that of the Cr<sub>1.7</sub>Mn<sub>1.3</sub>O<sub>4</sub> film (from a Cr<sub>2</sub>MnO<sub>4</sub> target), which shows that the average Mn oxidation state increases with Mn content. To quantify the Mn oxidation state, linear combination fitting of the film XANES spectra with Mn-containing reference compounds (Fe<sub>2</sub>MnO<sub>4</sub> and Mn<sub>3</sub>O<sub>4</sub>) was performed. Figure 2b and c shows the best fits for both CMO films. This shows that the Mn(III) fraction (Mn<sub>3</sub>O<sub>4</sub>) is higher for the Cr<sub>1.4</sub>Mn<sub>1.6</sub>O<sub>4</sub> film (fit Mn<sub>3</sub>O<sub>4</sub> = 38.6%) than for the Cr<sub>1.7</sub>Mn<sub>1.3</sub>O<sub>4</sub> film (fit Mn<sub>3</sub>O<sub>4</sub> = 20.3%), showing more Mn(III) in the Mn-richer film. Details are given in the Supporting Information. From the XANES, the average Mn oxidation state is  $2.13 \pm 0.12$  in the Cr<sub>1.7</sub>Mn<sub>1.3</sub>O<sub>4</sub> film and  $2.26 \pm 0.11$  in the Cr<sub>1.4</sub>Mn<sub>1.6</sub>O<sub>4</sub> film. This observation is consistent with the chemical shifts observed in the REXD (*vide infra*).

For the average Mn oxidation state determination, we also performed complementary nonresonant Mn K $\beta$  XES (Figure 2d and e). The K $\beta$  main lines (K $\beta$ <sub>1,3</sub> and K $\beta'$ ) correspond to the 3p  $\rightarrow$  1s core electron transitions, and their chemical sensitivity has an indirect origin through the electron–electron interactions and the core screening effect of the valence electrons.<sup>25,26</sup> To analyze these data, we account for the two likely Mn oxidation states, Mn(II) and Mn(III), by reconstructing the measured K $\beta$  main emission spectra using a linear combination of reference spectra measured with MnO and Mn<sub>2</sub>O<sub>3</sub> powders. This procedure gives an average oxidation state of  $2.25 \pm 0.04$  and  $2.33 \pm 0.04$  for the Cr<sub>1.7</sub>Mn<sub>1.3</sub>O<sub>4</sub> and



**Figure 2.** Spectroscopic results for two CMO films. (a) First derivatives of XANES near the Mn edge for the  $\text{Cr}_{1.7}\text{Mn}_{1.3}\text{O}_4$  and  $\text{Cr}_{1.4}\text{Mn}_{1.6}\text{O}_4$  CMO films and for two reference spinel oxides with Mn(II) and Mn(III) cations. The maximum indicates the edge position and is sensitive to the oxidation state of Mn species. Both CMO films exhibit an edge between  $\text{Fe}_2\text{MnO}_4$  (Mn oxidation state 2.0) and  $\text{Mn}_3\text{O}_4$  (average Mn oxidation state 2.67), as indicated by the red arrow. The XANES data and the best fits using a linear combination of the two Mn reference spectra are shown in part b for the  $\text{Cr}_{1.7}\text{Mn}_{1.3}\text{O}_4$  film and part c for the  $\text{Cr}_{1.4}\text{Mn}_{1.6}\text{O}_4$  film. XES spectra are shown in parts d and e for the  $\text{Cr}_{1.7}\text{Mn}_{1.3}\text{O}_4$  and  $\text{Cr}_{1.4}\text{Mn}_{1.6}\text{O}_4$  films, respectively. Mn(II) and Mn(III) contributions are based on the reference spectra measured with MnO and  $\text{Mn}_2\text{O}_3$  powders, respectively. The weak peak at low energy is the  $K\beta'$  line whereas the intense peak at the higher energy is the  $K\beta_{1,3}$ .



**Figure 3.** REXD of the  $\text{Cr}_{1.7}\text{Mn}_{1.3}\text{O}_4$  film. (a) REXD near the Mn K edge. Circles and crosses are the measured intensities for (422) and (222) reflections and are sensitive to  $Td$  and  $Oh$  sites, respectively. The blue and green lines are computed intensities using Mn form factors and  $f_1$  and  $f_2$  obtained from Mn(II)- and Mn(III)-containing oxides. The red solid and dashed lines indicate the REXD positions for Mn(III) and Mn(II), respectively. (b–e) Complete REXD for (222) and (422) reflections and the best fit structure factor (green lines). (b and c) Mn edge. (d and e) Cr edge. The four data sets are fit independently, and the best fit values are as follows:  $15\% \pm 2\%$  Mn on  $Oh$ ,  $100\% \pm 3\%$  Mn on  $Td$ ,  $85\% \pm 3\%$  Cr on  $Oh$ , and  $<3\%$  Cr on  $Td$  sites. We believe the sharp dip in the Cr (422) data (e) is due to an artifact, possibly trace Cr impurities in the detector filters.

$\text{Cr}_{1.4}\text{Mn}_{1.6}\text{O}_4$  films, respectively, consistent with the XANES results.

To quantitatively determine fractions of anti-site defects, REXD was carried out near Cr and Mn edges, and Figure 3 shows the results. Figure 3a contains the enlarged plots for the (222) and (422) peaks near the Mn edge of the  $\text{Cr}_{1.7}\text{Mn}_{1.3}\text{O}_4$  film and shows that the intensity minima appear at different energies for the two reflections. The observed minimum is mostly due to the minimum in  $f_1$ , where the resonance effect is the strongest.<sup>27</sup> Diffraction intensities for the (422) and (222) peaks are simulated using the atomic form factor ( $f_0$ ) of Mn cations and  $f_1$  and  $f_2$  extracted from the experimental XAS spectra of  $\text{Fe}_2\text{MnO}_4$  (with only Mn(II) cations) and  $\text{Mn}_2\text{O}_3$  (with only Mn(III) cations), assuming Mn(II) and Mn(III)

occupy the  $Td$  and  $Oh$  sites, respectively. The simulations are shown as lines in Figure 3a, where the minima and the fine structure above the edge, shift to higher energy for the higher cation oxidation state.

The 2 eV shift in the Mn-edge REXD minimum between the  $Td$ -site sensitive (422) data (at 6547 eV) and the  $Oh$ -site sensitive (222) data (at 6549 eV) shows the  $\text{Mn}_{Oh}$  have a higher oxidation state than  $\text{Mn}_{Td}$ . More importantly, the close similarity between the (422) experimental data and the simulation for Mn(II) (blue line) in Figure 3a is direct evidence that the  $\text{Mn}_{Td}$  are predominately Mn(II). Similarly, the close resemblance of the (222) data and the simulation for Mn(III) (green line) shows  $\text{Mn}_{Oh}$  are largely Mn(III).<sup>28</sup>

Parts b to e of Figure 3 shows the full data sets of (222) and (422) reflections for the  $\text{Cr}_{1.7}\text{Mn}_{1.3}\text{O}_4$  film. The circles are corrected integrated intensities, and the lines are best fits based on structure factor calculations using the fraction of Mn or Cr as the fitting variables. For  $Oh$  sites, the agreement between the data and the simulation is very good, with both data sets pointing to the same site occupancy:  $\text{Mn}_{Oh} = 15 \pm 2\%$  and  $\text{Cr}_{Oh} = 85 \pm 3\%$ . The  $Td$  sites are predominantly occupied by Mn ( $100\% \pm 3\%$ ), and there is little, if any,  $\text{Cr}_{Td}$ . The occupancies on the  $Td$  (or  $Oh$ ) site sum to unity, which indicates there is no cation vacancy within the accuracy of the measurement. We conclude that the Cr occupies <3% of the  $Td$  sites. REXD shows that this film, made from a nominally stoichiometric target, has excess Mn on the  $Oh$  sites, which is confirmed by XRF (see Table 2). The deviation from target stoichiometry is not surprising because it is predicted that CMO tends to form a Mn-rich compound that tolerates excess Mn on the  $Oh$  sites.<sup>16</sup> It is worth pointing out that the excess Mn(III) species on the  $Oh$  site are electrically neutral and do not generate charge carriers and contribute to conductivity.

We also performed REXD near the Mn edge for the  $\text{Cr}_{1.4}\text{Mn}_{1.6}\text{O}_4$  film. The same trend in the chemical shifts is observed where the minimum of the REXD spectrum in the (222) data is 2 eV above that for the (422) data. From fitting the REXD spectra (see Supporting Information for details), we determine that Mn(III) occupies 30% of the  $Oh$  sites and that Mn(II) occupies all the  $Td$  sites. The larger fraction of Mn(III) is in agreement with the larger Mn content measured by XRF and the higher average oxidation state obtained from the spectroscopy techniques (Figure 2).

For both films, the composition from XRF is similar to that from the REXD site occupancies. As discussed previously, this shows that the Mn on  $Td$  sites is predominately Mn(II), while, on the  $Oh$  sites, the Mn switches to Mn(III). Assuming all  $\text{Mn}_{Oh}$  is Mn(III) and all  $\text{Mn}_{Td}$  is Mn(II), we can compute the average Mn oxidation state from the site occupancies. For  $\text{Cr}_{1.7}\text{Mn}_{1.3}\text{O}_4$  and  $\text{Cr}_{1.4}\text{Mn}_{1.6}\text{O}_4$  films, the average oxidation states are 2.23 and 2.38, respectively. These values are in excellent agreement with those determined from XANES and XES within their margin of error (Table 2). This agreement strongly supports the conclusion that, in CMO spinels,  $\text{Mn}_{Td}$  remain (II) whereas the  $\text{Mn}_{Oh}$  are (III), making the anti-site defect charge neutral. Our experimental results are thus consistent with the DT theory, which predicts a change in cation oxidation state for the anti-site defects in a DT-4 spinel.

Although the conductivities of the CMO and GZO films are both below our measurement limit ( $10^{-4}$  S  $\text{cm}^{-1}$ ), the fundamentally different origins of the insulating behavior in these two prototypical DT materials can be elucidated from the spectroscopy and REXD. For  $\text{Ga}_2\text{ZnO}_4$ , there are equal concentrations of donor ( $\text{Ga}_{Td}$ ) and acceptor ( $\text{Zn}_{Oh}$ ) defect states and both are electrically active. However, the ionized defects compensate each other, resulting in an insulator. For CMO films, although one kind of anti-site defect ( $\text{Mn}_{Oh}$ ) is present in large quantities, it is electrically neutral because the Mn species are (III) on the  $Oh$  sites whereas on the  $Td$  sites they are (II). The net effect is that CMO is insulating. These conclusions are consistent with the doping type predictions and elucidate the fundamental difference between the two model materials representing DT-1 and DT-4 spinels.

## 5. CONCLUSION

In summary, we fabricated biaxially textured  $\text{Ga}_2\text{ZnO}_4$  and  $\text{Cr}_2\text{MnO}_4$  films and accurately determined their cation site occupancies and oxidation states and related these to the film electronic properties within the theoretical doping type (DT) framework. This framework classifies the electrical behavior of III–II spinels based on the anti-site defect concentrations and their energy levels. Our results for  $\text{Ga}_2\text{ZnO}_4$  and  $\text{Cr}_2\text{MnO}_4$  are consistent with theoretical predictions for DT-1 and DT-4 spinels, respectively. Combined with our previous report on a DT-2  $\text{Co}_2\text{ZnO}_4$ , we have provided experimental evidence to strongly support the doping type classification for spinel oxides and have shown the validity of this theoretical framework. Building on this now-confirmed understanding of the different spinel DTs and their defect chemistry, Design Principles (also known as Doping Rules) that target specific electrical properties using earth-abundant, spinel oxides can be developed. Given the large family of spinels and various combinations of transition metal cations, this creates a huge space for materials design.

More generally, the combination of resonant XRD and spectroscopic techniques demonstrated here allows quantitative analysis of site-specific occupancies and oxidation states of metal oxides containing several transition metal cations. When using a Materials by Design approach, such detailed information obtained on representative prototype materials is critical to validate the guiding theoretical principles (e.g., Doping Rules). Similar approaches can be adopted to study defect chemistry in other multiple transition cation systems for specific applications (e.g., electrode or electrolyte materials in batteries).

## ■ ASSOCIATED CONTENT

### 📄 Supporting Information

Review of the doping type theory, the target fabrication method, lab-source X-ray characterization of the biaxially textured films, and the detailed quantitative methods used for XAS, XRF, XES, as well as REXD analysis. This material is available free of charge via the Internet at <http://pubs.acs.org>.

## ■ AUTHOR INFORMATION

### Corresponding Author

\*E-mail: [mftoney@slac.stanford.edu](mailto:mftoney@slac.stanford.edu).

### Funding

This work is supported by the U.S. Department of Energy, Office of Science, Office of Basic Energy Sciences under Contract No. DE-AC36–08GO28308 to NREL as a part of the DOE Energy Frontier Research Center “Center for Inverse Design”. Portions of this research were carried out at the Stanford Synchrotron Radiation Lightsource (SSRL), a Directorate of SLAC National Accelerator Laboratory and an Office of Science User Facility operated for the U.S. Department of Energy Office of Science by Stanford University.

### Notes

The authors declare no competing financial interest.

## ■ ACKNOWLEDGMENTS

Y.S. acknowledges insightful discussions with Tula R. Paudel with regard to the doping type theory and with Lucian Pascut with regard to resonant diffraction. We thank Sean Brennan, John Bargar, Ronald Marks, Charles Troxel Jr., and Matthew

Latimer for their assistance at the SSRL beamlines and Andriy Zakutayev and Stephan Lany at NREL for helpful discussions.

## ■ REFERENCES

- (1) Rabe, K. M. *Annu. Rev. Condensed Matter Phys.* **2010**, *1*, 211–235.
- (2) Krupicka, S.; Novak, P. *Oxide Spinels in Handbook of Ferromagnetic Materials*; North-Holland Physics Publishing: Amsterdam, 1982; Vol. 3.
- (3) Another widely used way of writing the spinel chemical formula is  $AB_2O_4$ . We, however, write  $A_2BO_4$ , which is common for spinels with formal cation valencies  $Z_A = 2$  and  $Z_B = 4$ , such as  $Mg_2TiO_4$ . The main reason for our choice is because the work presented here is part of a larger project that treats all  $A_2BX_4$  compounds (not only spinels) in different structure types, including olivine  $Fe_2SiO_4$ ,  $\beta$ - $K_2SO_4$ , or  $La_2CuO_4$ , for which  $A_2BX_4$  is the generally used notation.
- (4) Zhang, S. B.; Wei, S. H. *Appl. Phys. Lett.* **2002**, *80*, 8.
- (5) Owings, R. R.; Exarhos, G. J.; Windisch, C. F.; Holloway, P. H.; Wen, J. G. *Thin Solid Films* **2005**, *483* (1–2), 175–184.
- (6) Kawazoe, H.; Yanagi, H.; Ueda, K.; Hosono, H. *MRS Bull.* **2000**, *25* (8), 28–36.
- (7) Markovsky, B.; Talyossef, Y.; Salitra, G.; Aurbach, D.; Kim, H. J.; Choi, S. *Electrochem. Commun.* **2004**, *6*, 8.
- (8) Alcantara, R.; Jaraba, M.; Lavela, P.; Tirado, J. L. *Chem. Mater.* **2002**, *14* (7), 2847.
- (9) Suzuki, Y. *Annu. Rev. Mater. Res.* **2001**, 31.
- (10) Luders, U.; Barthelemy, A.; Bibes, M.; Bouzouane, K.; Fusil, S.; Jacquet, E.; Contour, J.-P.; Bobo, J.-F.; Fontcuberta, J.; Fert, A. *Adv. Mater.* **2006**, *18*, 13.
- (11) Mayhew, L. E.; Ellison, E. T.; McCollom, T. M.; Trainor, T. P.; Templeton, A. S. *Nat. Geosci.* **2013**, *6*, 478.
- (12) Muhich, C. L.; Evanko, B. W.; Weston, K. C.; Lichty, P.; Liang, X.; Martinek, J.; Musgrave, C. B.; Weimer, A. W. *Science* **2013**, *341* (6145), 540–542.
- (13) Kumar, P. V.; Short, M. P.; Yip, S.; Yildiz, B.; Grossman, J. C. *J. Phys. Chem. C* **2013**, *117* (11), 5678–5683.
- (14) Ellmer, K.; Klein, A.; Rech, B., Eds.; *Transparent conductive zinc oxide—basics and applications in thin film solar cells*; Springer: Berlin, 2008.
- (15) Xiao, J.; Chen, X.; Sushko, P. V.; Sushko, M. L.; Kovarik, L.; Feng, J.; Deng, Z.; Zheng, J.; Graff, G. L.; Nie, Z.; Choi, D.; Liu, J.; Zhang, J.-G.; Whittingham, M. S. *Adv. Mater.* **2012**, *24*, 16.
- (16) Paudel, T. R.; Zakutayev, A.; Lany, S.; d’Avezac, M.; Zunger, A. *Adv. Funct. Mater.* **2011**, *21* (23), 4493–4501.
- (17) Perry, N. H.; Mason, T. O.; Ma, C.; Navrotsky, A.; Shi, Y.; Bettinger, J. S.; Toney, M. F.; Paudel, T. R.; Lany, S.; Zunger, A. *J. Solid State Chem.* **2012**, *190*, 143–149.
- (18) Ndione, P. F.; Shi, Y.; Stevanovic, V.; Zakutayev, A.; Lany, S.; Parilla, P. A.; Perkins, J. D.; Berry, J. J.; Ginley, D. S.; Toney, M. F. *Adv. Funct. Mater.* **2013**, DOI: 10.1002/adfm.201302535.
- (19) Perkins, J. D.; Paudel, T. R.; Zakutayev, A.; Ndione, P. F.; Parilla, P. A.; Young, D. L.; Lany, S.; Ginley, D. S.; Zunger, A.; Perry, N. H.; Tang, Y.; Grayson, M.; Mason, T. O.; Bettinger, J. S.; Shi, Y.; Toney, M. F. *Phys. Rev. B* **2011**, *84*, 20.
- (20) Ravel, B.; Newville, M. *J. Synchrotron Radiat.* **2005**, *12*, 537–541.
- (21) Sokaras, D.; Weng, T.-C.; Nordlund, D.; Alonso-Mori, R.; Velikov, P.; Wagner, D.; Garachtchenko, A.; George, M.; Borzenets, V.; Johnson, B.; Rabedeau, T.; Bergmann, U. *Rev. Sci. Instrum.* **2013**, *84*, 053102.
- (22) Waseda, Y. *Anomalous X-ray scattering for materials characterization: atomic-scale structure determination*; Springer-Verlag Berlin Heidelberg: Berlin, Germany, 2002.
- (23) Pickering, I. J.; Sansone, M.; Marsch, J.; George, G. N. *J. Am. Chem. Soc.* **1993**, *115*, 14.
- (24) Martinez-Lope, M. J.; Retuerto, M.; de la Calle, C.; Porcher, F.; Alonso, J. A. *J. Solid State Chem.* **2012**, *187*, 172–176.
- (25) Glatzel, P.; Bergmann, U. *Coord. Chem. Rev.* **2005**, *249* (1–2), 65–95.
- (26) Bergmann, U.; Glatzel, P. *Photosynth. Res.* **2009**, *102* (2–3), 255–266.
- (27) Materlik, G.; Sparks, C. J.; Fischer, K., Eds.; *Resonant anomalous X-ray scattering theory and applications*; North Holland: 1994.
- (28) The hump near 6565 eV in the (222) data is not well captured in the simulation (green line) because the Mn(III) in the  $Mn_2O_3$  reference has a different local environment than the  $Mn_{Oh}$  in a spinel oxide. There is a better agreement for the Td site data (circles and blue line), since both the CMO thin film and the  $Fe_2MnO_4$  reference have a spinel structure.